Chemometrics and Intelligent Laboratory Systems 105 (2011) 7–18

Contents lists available at ScienceDirect

Chemometrics and Intelligent Laboratory Systems

journal homepage: www.elsevier.com/locate/chemolab

Joint processing of the parallel and crossed polarized Raman spectra and uniqueness in blind nonnegative source separation

S. Miron [a,*], M. Dossot [b], C. Carteret [b], S. Margueron [c], D. Brie [a]

[a] CRAN, Nancy-Université, CNRS, Boulevard des Aiguillettes, B. P. 239, F-54506,Vandœuvre-lès-Nancy, France
[b] LCPME, Nancy-Université, CNRS, 405 rue de Vandœuvre, F-54600, Villers-lès-Nancy, France
[c] LMOPS, EA 4423, Université Paul Verlaine - Metz, 2 rue Eduard Belin, 57070, Metz, France

ARTICLE INFO

Article history:
Received 18 May 2010
Received in revised form 11 October 2010
Accepted 22 October 2010
Available online 30 October 2010

Keywords:
Raman spectroscopy
Polarization
Raman imaging
Nonnegative mixture identifiability
Uniqueness
MCR
NMF
PARAFAC

ABSTRACT

Polarization analysis in Raman spectroscopy provides a powerful tool in chemical physics to identify the symmetry of the vibration modes of molecules, macromolecules and crystals, according to their crystallographic structure and local spatial orientation. In this paper we propose two new approaches in polarized Raman spectroscopy for data with rotational and spatial diversity, respectively. We show that the joint use of parallel and crossed polarization data yields more accurate source separation results and improves the uniqueness properties of the solution in blind nonnegative source separation algorithms. The proposed approaches are validated on two real polarized Raman data sets.

1. Introduction

Raman scattering is a light–matter interaction process which reflects the molecular vibration properties of molecules and materials thus characterizing the chemical composition of the analyzed sample [1,2]. When coupled with a confocal microscope having motorized stages, Raman spectra can be recorded at each (x,y) point on a sample grid, yielding Raman mapping [3]. For materials presenting a regular atomic or molecular structure, a more accurate characterization of the sample can be achieved by using polarizers [4]. In particular, this is the case for crystals as their response to the polarized light excitation will reflect the crystallographic structure of the sample, motivating the development of polarized Raman spectroscopy and mapping.

In most cases the incident laser beam is linearly polarized and the Raman scattered light can be recorded in parallel or perpendicular directions by a polarized analyzer. In this paper two polarized data acquisition schemes are considered. They are respectively referred to as *rotational diversity*[1] and *spatial diversity* data acquisition. The multidimensional signals recorded this way must be processed in order to get insights into the physico-chemical properties of the analyzed sample. Information about the local orientation of the sample under the microscope objective, through the retrieval of the local components of the Raman polarizability tensor [5], can thus be obtained.

Due to the multivariate nature of the data, a model which is now widely spread in spectroscopy consists in considering the data as a mixture of pure components referred to as sources, whose concentrations are varying with respect to some physical parameter referred to as diversity. The data processing consists in the retrieval of these sources and their concentrations. This problem is called *multivariate curve resolution (MCR)* [6] in chemometrics while in the literature of signal processing it is called *nonnegative source separation* or *nonnegative matrix factorization (NMF)* [7,8]. The *nonnegative* prefix is used to stipulate the fact that source spectra and concentrations are positive by nature.

In this paper, two signal processing models for the Raman polarized spectra, acquired with angular and spatial diversity, are proposed.

* Corresponding author. Tel.: +33 383684469.
E-mail addresses: sebastian.miron@cran.uhp-nancy.fr (S. Miron), manuel.dossot@lcpme.cnrs-nancy.fr (M. Dossot), cedric.carteret@lcpme.cnrs-nancy.fr (C. Carteret), margueron_sam@metz.supelec.fr (S. Margueron), david.brie@cran.uhp-nancy.fr (D. Brie).

[1] *N.B.* Not to be confused with *rotational ambiguity* which refers to the non-uniqueness of data decomposition into subspaces.

0169-7439/$ – see front matter © 2010 Elsevier B.V. All rights reserved.
doi:10.1016/j.chemolab.2010.10.005

In the case of angular diversity data, physical considerations yield a bilinear mixture model. In chemometrics, the NMF problem is classically solved using the multivariate curve resolution-alternating least squares (MCR-ALS) method [6]. SIMPLISMA-like techniques [9], based on the strong pure-variable assumption, are employed to initialize the MCR-ALS algorithm. In signal processing community, another popular technique is the NMF algorithm, introduced by Lee and Seung in [8], using a multiplicative updating rule to solve the NMF problem. However, even if in practice these methods give generally good results, because of the so-called rotational ambiguities, most of the time, uniqueness of the decomposition cannot be guaranteed.

Getting back to the case of polarized Raman spectroscopy, both polarizations are generally recorded but they are processed separately. One of the main contributions of this paper is to show that the joint processing of both polarization spectra can reduce significantly the rotational ambiguities. However, as the solution still cannot be guaranteed to be unique, we use in the experimental part the BPSS (Bayesian Positive Source Separation) method [10,11] which ensures, through the assignment of Gamma priors on the distributions of both the source signals and the mixing coefficients, the positiveness and uniqueness of the solution. To some extent, this algorithm shares some similarities with the *positive matrix factorization (PMF)* approach introduced in [7].

For the spatial diversity case, based upon physical considerations, we propose a trilinear Candecomp/Parafac (CP) model of the data [12,13]. One of the main interests of this model is that its uniqueness is ensured under mild conditions. In that respect, the fitting of this three-way model, which is classically achieved by the ALS algorithm [13], is not as challenging as in the bilinear case. However, even for trilinear data, imposing positivity constraints to the ALS algorithm may result in improved convergence properties.

The rest of the paper is organized as follows: in Section 2 the principles of polarized Raman data acquisition are briefly illustrated, in Section 3 we present the model and the fitting algorithms for the rotational diversity polarized data and in Section 4 the same thing is done for the Raman imaging data. Section 5 presents results of the proposed approaches on real spectra and some concluding remarks are given in Section 6.

2. Polarized data acquisition

The Raman measurements were carried out in back scattering geometry with the same objective for excitation and collection of light. The confocal Raman spectrometer was equipped with a cooled CCD camera and the laser source was an ionized argon laser emitting at a wavelength $\lambda = 514.5$ nm. The analyzed crystal sample is fixed on a rotating stage as shown in Fig. 1. Two coordinate systems are used, one associated with the laboratory space-fixed coordinates (O,X,Y,Z) and another attached to the analyzed sample (O,x,y,z). The incident light is polarized such that the electric field arriving on the sample is oriented along the Y direction. The scattered light is analyzed by positioning an analyzer in front of the entrance slit of the spectrometer. The analyzer is oriented either along the Y-axis (*parallel polarization*) or the X-axis (*crossed polarization*). Thus, the acquisition in one point of the sample yields a pair of spectra, one for the parallel polarization, indexed by Y and another for the crossed polarization, indexed by X.

Depending on the application, two acquisition schemes can be envisaged. The *rotational diversity* scheme consists in rotating the sample around the Z-axis (Fig. 1) with a fixed angular step (typically 10°) and acquiring two polarized spectra for each step of the rotation. This type of acquisition is mainly used to characterize the *polarizability tensor* (see Subsection 2.1) of the analyzed crystal sample system. Another acquisition scheme, used in Raman microscopy mapping, is the *spatial diversity*. It consists in recording polarized spectra with point-by-point scanning mode over a chosen sample area with a fixed step. This procedure permits to obtain maps of the spatial distribution of a particular component within mixture of the analyzed sample.

2.1. Physical considerations

To develop the mathematical models for the polarized Raman data, it is necessary to briefly remind the physical phenomenon related to Raman scattering of polarized light. A useful quantity in this context is the *polarizability tensor*. The polarizability tensor is a 3×3 real-valued matrix $\boldsymbol{\alpha}$, relating the induced electric dipole moment $\mathbf{p}$ in the crystal to the electric field vector $\mathbf{e}$ of the incident light. In the crystal-fixed

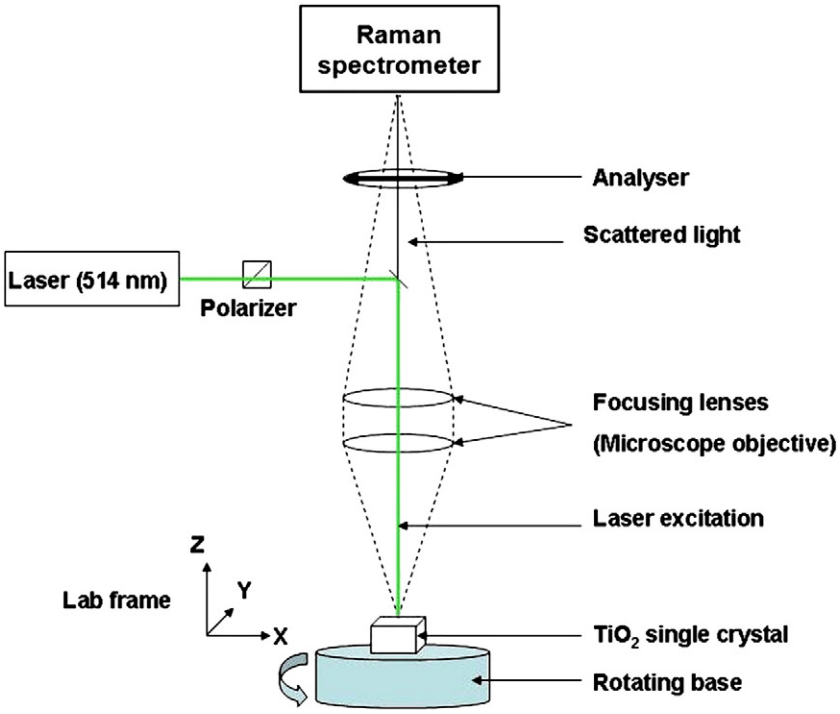

Fig. 1. Polarized Raman spectroscopy set-up in backscattering geometry.

coordinate system (O,x,y,z) the polarizability tensor can be written as:

$$\boldsymbol{\alpha} = \begin{pmatrix} \alpha_{xx} & \alpha_{xy} & \alpha_{xz} \\ \alpha_{yx} & \alpha_{yy} & \alpha_{yz} \\ \alpha_{zx} & \alpha_{zy} & \alpha_{zz} \end{pmatrix}. \quad (1)$$

A Raman polarizability tensor is associated to a particular *vibrational mode* for a given crystal orientation [1,2]. The vibrational modes will be thought of as sources in the source separation problems presented in this paper. As the measurements are performed in the laboratory coordinates system (O,X,Y,Z), a rotation matrix $\mathbf{R}(\phi,\theta,\chi)$ [1,2], accounts for the coordinate system change between the sample and the laboratory frames. Denoting the Euler angles describing the sample rotations in the coordinate system (O,X,Y,Z) by $\boldsymbol{\theta}=(\phi,\theta,\chi)$, the induced electric vector in non polar crystal can be expressed by the tensorial change of basis:

$$\mathbf{p}(\boldsymbol{\theta}) = \mathbf{R}^T(\boldsymbol{\theta})\boldsymbol{\alpha}\ \mathbf{R}(\boldsymbol{\theta})\mathbf{e}. \quad (2)$$

If we denote by p_X, p_Y, p_Z, the three components of $\mathbf{p}$ along X, Y and Z axes, the intensity of the scattered light, measured by the spectrometer, is given by the following proportionality relationship:

$$\mathbf{i}(\boldsymbol{\theta}) = \begin{pmatrix} i_X & i_Y & i_Z \end{pmatrix}^T \propto \begin{pmatrix} p_X^2 & p_Y^2 & p_Z^2 \end{pmatrix}^T. \quad (3)$$

In practical applications in backscattering geometry only i_X and i_Y are measured, corresponding to the crossed and parallel polarizations, respectively.

We will suppose in the following that the recorded scattered light is a mixture of N sources and that K wavelengths/wavenumbers are acquired for each spectrum in one point on the crystal surface.

3. Rotational diversity data

In this section we focus on the angular diversity data whose model is based on the physico-chemical knowledge on the analyzed crystal sample, expressed by the non-zero components of the polarizability tensor.

3.1. The bilinear model

For the rotational diversity acquisition scheme, M polarized spectra are acquired for M different rotation angles $(\boldsymbol{\theta}_1,\ldots,\boldsymbol{\theta}_M)$ of the analyzed sample. For this angular diversity data, the "sources" are represented by vibrational modes. Indeed, the vibrational modes are characterized by specific displacements of the atoms from their equilibrium position, which dictate the magnitude of the components of the Raman polarizability tensor. The change of polarized Raman intensity versus rotational angle, for a specific vibrational mode, will therefore be different from another one. Each mode in polarized Raman spectra will thus contribute as one source in the full spectrum.

Under the generally accepted assumption of instantaneous linear mixture, the acquired data can be structured as two $M\times K$ matrices, corresponding to the two polarization orientations X and Y:

$$\mathbf{D}_p = \mathbf{A}_p\mathbf{S}_p^T + \mathbf{E}_p \quad \text{with} \quad p = X, Y. \quad (4)$$

In Eq. (4), matrix $\mathbf{E}_p \in \mathbb{R}^{M\times K}$ accounts for the additive noise on the sensors and the model errors and

$$\mathbf{A}_p = \begin{pmatrix} i_{1,p}(\boldsymbol{\theta}_1) & \cdots & i_{N,p}(\boldsymbol{\theta}_1) \\ \vdots & \ddots & \vdots \\ i_{1,p}(\boldsymbol{\theta}_M) & \cdots & i_{N,p}(\boldsymbol{\theta}_M) \end{pmatrix} \in \mathbb{R}^{M\times N}, \quad (5)$$

$$\mathbf{S}_p = \begin{pmatrix} s_{1,p}(\lambda_1) & \cdots & s_{N,p}(\lambda_1) \\ \vdots & \ddots & \vdots \\ s_{1,p}(\lambda_K) & \cdots & s_{N,p}(\lambda_K) \end{pmatrix} \in \mathbb{R}^{K\times N}. \quad (6)$$

are two matrices containing on their columns the angular and the spectral evolution of the scattered light for each one of the N sources, respectively, and for the two polarization orientations. Thus, Eq. (4) illustrates two bilinear models for the two polarization types, leading *a priori* to two independent source separation problems.

However, if we further analyze the underlying physico-chemical phenomenon generating the two data sets, it can be observed that the spectra of pure compounds are the same for the crossed and the parallel polarization [1,2], since the vibrational modes are imposed by the structure of the crystal. This implies $\mathbf{S}_X=\mathbf{S}_Y=\mathbf{S}$, which is quite intuitive if we consider a geometrical point of view in which the crossed and parallel polarized spectra are projections of the same signal on two orthogonal axes. By injecting this information into Eq. (4), one gets:

$$\begin{pmatrix} \mathbf{D}_X \\ \mathbf{D}_Y \end{pmatrix} = \begin{pmatrix} \mathbf{A}_X \\ \mathbf{A}_Y \end{pmatrix}\mathbf{S}^T + \begin{pmatrix} \mathbf{E}_X \\ \mathbf{E}_Y \end{pmatrix}. \quad (7)$$

Eq. (7) points out a bilinear model for the polarized spectra with rotational diversity considering both polarized spectra families jointly. Besides the fact that this is a more natural and compact representation of the data, the sample size is doubled in Eq. (9) compared to Eq. (4) which should normally improve the accuracy of the estimated source parameters.

In order to simplify the presentation we use the following notations:

$$\mathbf{D} = \begin{pmatrix} \mathbf{D}_X \\ \mathbf{D}_Y \end{pmatrix}, \quad \mathbf{A} = \begin{pmatrix} \mathbf{A}_X \\ \mathbf{A}_Y \end{pmatrix}, \quad \mathbf{E} = \begin{pmatrix} \mathbf{E}_X \\ \mathbf{E}_Y \end{pmatrix}. \quad (8)$$

Eq. (7) can thus be re-written in a more concise manner as:

$$\mathbf{D} = \mathbf{A}\mathbf{S}^T + \mathbf{E}. \quad (9)$$

Given the nature of the data, the sources and the mixing coefficients are positive-valued, meaning that Eq. (9) expresses a NMF (Nonnegative Matrix Factorization) model [7]. It should be noticed that stacking the data matrices $\mathbf{D}_X$ and $\mathbf{D}_Y$ into a bigger matrix $\mathbf{D}$ can also be seen as a data augmentation strategy. This kind of technique has already been proposed for diverse problems such as the analysis of multiple runs of gasoline blending processes [14]. Another example is the joint analysis of UV–visible spectra related to the complexation of the aluminum by caffeic acid and the titration of caffeic acid [15]. Actually, the benefit of matrix augmentation strategy is threefold: it allows to decrease estimation error uncertainties, it may remove rank deficiency and helps in reducing rotational ambiguities. Hereafter, we mainly focus on the reduction of rotational ambiguities. We also provide a geometrical interpretation of the uniqueness of NMF model, giving insights into how matrix augmentation may reduce rotational ambiguities.

3.2. Identifiability of the NMF mixture model

A source mixture model is *identifiable* if the sources can be uniquely estimated (up to permutation and scaling indeterminacies) from the observations. In order to discuss the identifiability of the NMF model (Eq. (9)) the notion of *simplicial cone* needs to be introduced.

Definition 1 (Simplicial cone). The simplicial cone generated by a family of vectors $\{\mathbf{s}_n\}_{n=1}^N$ is

$$\mathcal{C}(\{\mathbf{s}_n\}) = \left\{\mathbf{x} : \mathbf{x} = \sum_n \alpha_n\mathbf{s}_n, \alpha_n > 0\right\}.$$

The order of a simplicial cone is the dimension of the subspace span $(\{\mathbf{s}_n\}_{n=1}^N)$.

Based on the simplicial cone, a necessary and sufficient condition for NMF identifiability has been provided by Chen in [16]:

Theorem 1 (Necessary and sufficient unicity condition). *Denoting $\mathcal{K}$ the convex hull of the data matrix $\mathbf{X}$, the decomposition of $\mathbf{X}$ according to $\mathbf{X}=\mathbf{AS}^T$, $\mathbf{A}\geq 0$, $\mathbf{S}\geq 0$ is unique if and only if the simplicial cone $\mathcal{C}(\mathbf{S})$, such as $\mathcal{K}\subset\mathcal{C}(\mathbf{S})$, is unique.*

Clearly, Theorem 1 does not provide any numerical conditions to check if a NMF is unique or not. This motivated the work of [17,18] from which it appears that uniqueness relies on the number of zero entries in both matrices $\mathbf{A}$ and $\mathbf{S}$. When uniqueness is not achieved, there is a set of possible solutions, referred to as admissible solutions or rotational ambiguities. The set of admissible solutions can be determined analytically [19] for the special case of two sources. The reader is also referred to [20] where a complete characterization of the rotational ambiguities arising in the two-component case is proposed. As mentioned in [20], the case of more than two components is significantly more complex. In Ref. [10] the determination of the admissible solutions for the three component problem was addressed through numerical simulations. However, such an approach is case dependent and requires high computation time. In this section we provide a geometrical interpretation of the set of admissible solutions which is used to explain why the joint use of parallel and crossed polarization data (and generally any matrix augmentation strategy) is expected to improve the NMF problem in the sense of reducing the set of admissible solutions and thus, the rotational ambiguities.

For simplicity and without loss of generality, we restrain our explanations to the case of three sources, as illustrated in Section 5 on real data. Consider the NMF noiseless model:

$$\mathbf{D}=\mathbf{AS}^T \quad \text{with} \quad \mathbf{A}\in\mathbb{R}^{M\times 3} \quad \text{and} \quad \mathbf{S}\in\mathbb{R}^{K\times 3}. \tag{10}$$

Each raw of data matrix $\mathbf{D}$ can be seen as a point in a K-dimensional space. The fact that the data are nonnegative means that every such point lies in the positive orthant $\mathbb{R}_+^K$ of $\mathbb{R}^K$. The factorization (Eq. (10)) implies that all the raws of $\mathbf{D}$ lie in the simplicial cone generated by the columns of $\mathbf{S}$, namely $\mathcal{C}(\mathbf{s}_1,\mathbf{s}_2,\mathbf{s}_3)$. Thus, the admissible solutions for $(\mathbf{s}_1,\mathbf{s}_2,\mathbf{s}_3)$ are confined in the three-dimensional subspace obtained as the intersection of $\mathbb{R}_+^K$ with span($\mathbf{S}$). Let $\{\mathbf{e}_1,\mathbf{e}_2,\mathbf{e}_3\}$ be a canonical unitary basis of $\mathbb{R}_+^K\cap$span($\mathbf{S}$) (the vectors $\mathbf{e}_1,\mathbf{e}_2,\mathbf{e}_3$ are contained in the canonical planes of $\mathbb{R}^K$), then all the data lie inside $\mathcal{C}(\mathbf{s}_1,\mathbf{s}_2,\mathbf{s}_3)$ (Fig. 2).

In Fig. 3 we consider a mapping (affine projection) of the three-dimensional space to the plane $(1,1,1)$. By this mapping, a plane in $\mathbb{R}^3$ is

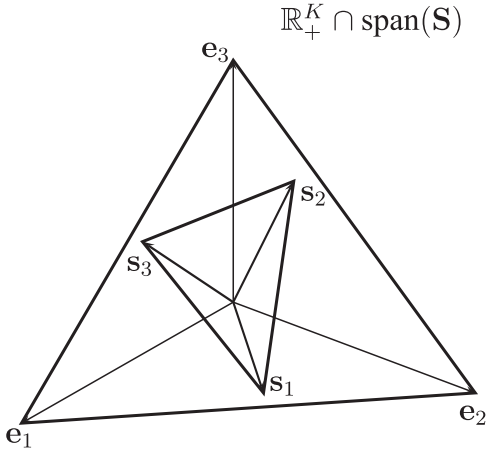

Fig. 2. Geometrical illustration of $\mathbb{R}_+^K\cap$span($\mathbf{S}$). The vectors $\mathbf{e}_1,\mathbf{e}_2,\mathbf{e}_3$ form a canonical unitary basis and $\mathbf{s}_1,\mathbf{s}_2,\mathbf{s}_3$ are the sources.

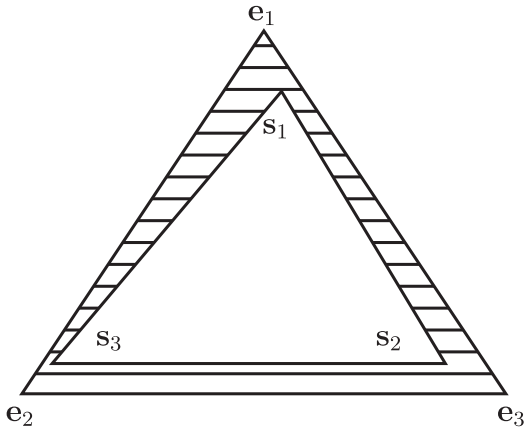

Fig. 3. Mapping to the plane $(1,1,1)$ of the three-dimensional space. The hatched area corresponds to the admissible solutions domain.

mapped to a line and a simplicial cone is mapped to a triangle. Let us suppose first that there are enough data to fully cover the triangle ($\mathbf{s}_1$, $\mathbf{s}_2$,$\mathbf{s}_3$). Then any third order simplicial cone including $\mathcal{C}(\mathbf{s}_1,\mathbf{s}_2,\mathbf{s}_3)$ (the hatched area in Fig. 3) is an admissible solution for NMF (Eq. (10)). This means that the problem is intrinsically ill-posed and the only sources that can be uniquely recovered are those overlapping with one of the basis vectors ($\mathbf{e}_1,\mathbf{e}_2,\mathbf{e}_3$). The regularization of the problem by imposing sparseness constraints on the sources [21] reduces the solution space by dragging ($\mathbf{s}_1,\mathbf{s}_2,\mathbf{s}_3$) towards the basis vectors.

Suppose now that $\mathcal{C}(\mathbf{s}_1,\mathbf{s}_2,\mathbf{s}_3)$ is the same as $\mathcal{C}(\mathbf{e}_1,\mathbf{e}_2,\mathbf{e}_3)$, meaning that the hatched area on Fig. 3 vanishes. Suppose also that the data points do not fill completely $\mathcal{C}(\mathbf{s}_1,\mathbf{s}_2,\mathbf{s}_3)$ (Fig. 4). Then, any third order simplicial cone containing all the data is an admissible solution to problem. A sufficient condition for uniqueness, presented in [17], is to have at least two data points on each of the three edges of the triangle ($\mathbf{s}_1,\mathbf{s}_2,\mathbf{s}_3$). In this case there is only one third order simplicial cone, namely $\mathcal{C}(\mathbf{s}_1,\mathbf{s}_2,\mathbf{s}_3)$, that includes all the observations. In general, the size of the admissible solutions set depends on the coverage degree of the triangle ($\mathbf{s}_1,\mathbf{s}_2,\mathbf{s}_3$) by the data points. The better the data covers the triangle the smaller the solution set. This explains the improvements in the NMF admissible solutions obtained in Section 5 by the joint use of crossed and parallel polarization data sets. Because different sources (vibrational modes) are characterized by different polarizability tensors it means that the sources present distinct behaviors in at least one polarized data set. Thus, it is highly probable that the observed mixtures for the crossed and parallel polarizations cover distinct areas of the simplicial cone $\mathcal{C}(\mathbf{s}_1,\mathbf{s}_2,\mathbf{s}_3)$. An intuitive geometrical interpretation is given in Fig. 4, where convex hulls of the two data sets (crossed and parallel) are represented by a dashed and a dotted line, respectively. It is obvious that by using both data sets jointly the incertitude on the sources (the shadowed area) is reduced compared to one set only. This result is illustrated in Section 5 where NMF is applied on real data in several runs with different initial values.

By imposing sparseness on the mixing coefficients, the solution given by the smallest simplicial cone $\mathcal{C}(\mathbf{d}_1,\mathbf{d}_2,\mathbf{d}_3)$ is favored. Sparseness on both sources and mixing coefficients would give an intermediate solution between $\mathcal{C}(\mathbf{d}_1,\mathbf{d}_2,\mathbf{d}_3)$ and $\mathcal{C}(\mathbf{e}_1,\mathbf{e}_2,\mathbf{e}_3)$. In chemometrics, other constraints, such as unimodality or *a priori* known components are used. Let us also mention concentration selectivity which is, to some extent, related to imposing sparseness on the mixing coefficients. We did not study this point further since it is out of the scope of the present paper.

3.3. Fitting the rotational diversity data

For the direct model expressed by Eq. (7), the inverse problem consists in estimating $\mathbf{A}_X,\mathbf{A}_Y$ and $\mathbf{S}$ knowing $\mathbf{D}_X$ and $\mathbf{D}_Y$. Note that once

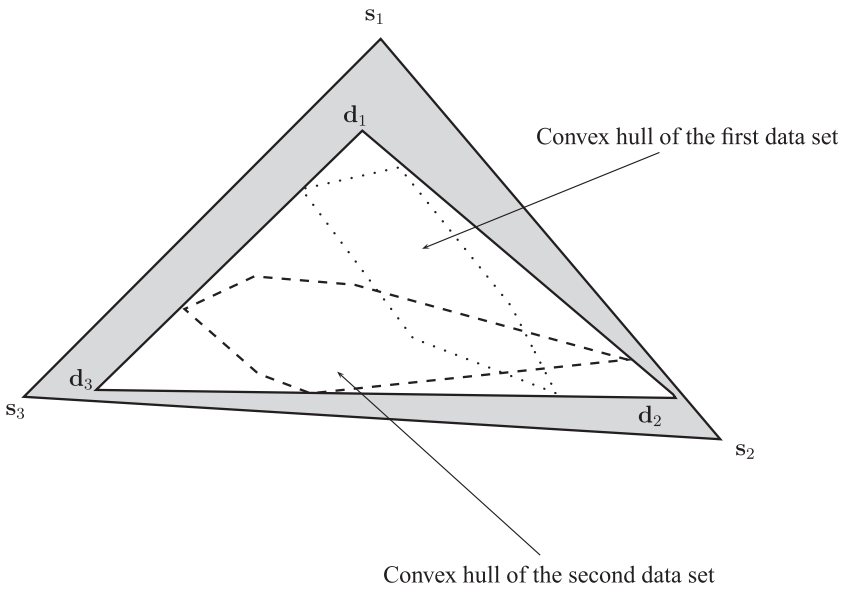

Fig. 4. Illustration of the indeterminacy due to the mixing coefficients. The dotted area and the dashed area represent the crossed and parallel polarization data sets, and $\mathcal{C}(\mathbf{d}_1,\mathbf{d}_2,\mathbf{d}_3)$ is the simplicial cone containing the maximum number of data points on its facets.

the matrix **A** in Eq. (9) is estimated, it is straightforward to obtain $\mathbf{A}_X$ and $\mathbf{A}_Y$.

Alternating Least Squares (ALS) algorithms with non-negativity constraints are generally used to estimate the matrices **A** and **S**. A basic approach to invert the NMF model (9) is given in Algorithm 1. A large number of methods improving the performances of this basic approach have been proposed lately in the literature. One of the most popular is the NMF algorithm by Lee and Seung [8], using a multiplicative updating rule. For more details about these techniques see [22] and the references therein.

Algorithm 1. Basic approach to estimate NMF model parameters

1: INPUT: the observation matrix **D** and the number of the sources N
2: Initialize the matrix **A** randomly, or by using a deterministic strategy
3: Fix ε to a small positive value (typically, 10^{-16})
4: **repeat**
5: Estimate **S**: $\mathbf{S}=\max\{\varepsilon,\mathbf{D}^T\mathbf{A}(\mathbf{A}^T\mathbf{A})^{-1}\}$,
where $(\cdot)^T$ denotes the transposed of a matrix
6: Update **A**: $\mathbf{A}=\max\{\varepsilon,\mathbf{DS}(\mathbf{S}^T\mathbf{S})^{-1}\}$,
7: **until** convergence
8: OUTPUT: estimates of **A** and **S**.

4. Spatial diversity data

We propose in this section a model for Raman imaging data using both crossed and parallel polarized lights. The details of the Raman imaging acquisition have been presented in Section 2.

4.1. The trilinear model

For the spatial diversity scheme, two polarized spectra are acquired in L different points denoted by: $d_1,...,d_L$, on a regular spatial grid. Define the following matrices:

$$\mathbf{P}=\begin{pmatrix} i_{1,X} & \cdots & i_{N,X} \\ i_{1,Y} & \cdots & i_{N,Y}\end{pmatrix}\in\mathbb{R}^{2\times N}, \tag{11}$$

$$\mathbf{B}=\begin{pmatrix} b_1(d_1) & \cdots & b_N(d_1) \\ \vdots & \ddots & \vdots \\ b_1(d_L) & \cdots & b_N(d_L)\end{pmatrix}\in\mathbb{R}^{L\times N}. \tag{12}$$

The **B** matrix contains on its columns the spatial evolution of the source concentrations and **P** characterizes the behavior of the N sources for the two polarization orientations. The acquired data can thus be expressed as two $L\times K$ matrices:

$$\mathbf{W}_p=\mathbf{B}\mathcal{D}_p(\mathbf{P})\mathbf{S}^T+\mathbf{E}_p,\quad p=X,Y, \tag{13}$$

where $\mathcal{D}_p(\mathbf{P})=\mathtt{diag}(i_{1,p},...,i_{N,p})$ is a diagonal matrix which takes the first or the second row of **P** as its diagonal, and $\mathbf{E}_p\in\mathbb{R}^{L\times K}$ the noise matrix. Relation (13) clearly expresses a three-way CANDECOMP/PARAFAC (CP) model [13] for the polarized data with spatial diversity. Fig. 5 illustrates the three-dimensional structure of the data.

The trilinear model validity is conditioned by the invariance of the source polarization behavior with respect to spatial displacement. In practice, this is the case if i) the analyzed objects have well-defined spatial orientation and their size is bigger than the laser spot or ii) they

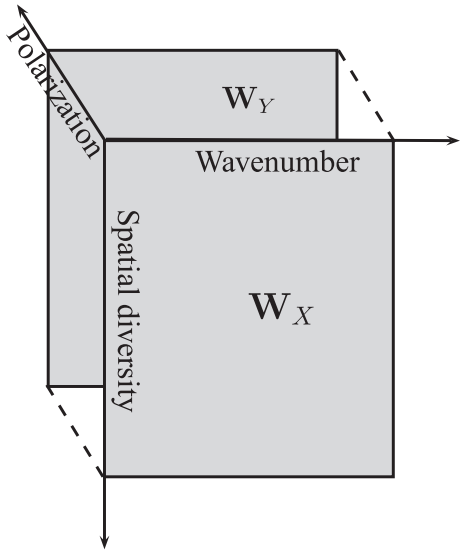

Fig. 5. Illustration of the three-way data structure and the corresponding diversities.

have random orientation and their size is largely inferior to the laser spot.

4.2. Identifiability issues for the trilinear model

Before presenting the algorithms for fitting the spatial diversity data, identifiability conditions for the trilinear mixture model expressed by Eq. (13) must be discussed. The spatial acquisition scheme yields a trilinear CP model as one can see in Eq. (13). The inverse problem for this model is the estimation of **B**,**S** and **P** from the observations $\mathbf{W}_p$. Unlike bilinear mixtures, the identifiability of a CP model is ensured under mild constraints given by *Kruskal's condition* [23]. Before stating the identifiability condition for the presented trilinear model, the *Kruskal-rank* of a matrix must be defined.

Definition 2 (Kruskal-rank). The Kruskal-rank of a matrix **B** equals r ($k_{\mathbf{B}}=r$), if every r columns of **B** are linearly independent but this does not hold for $r+1$ columns.

Applied to our case, Kruskal's condition states that one can uniquely estimate the matrices **B**,**S** and **P** in Eq. (13) if:

$$k_{\mathbf{B}} + k_{\mathbf{S}} + k_{\mathbf{P}} \geq 2(N+1). \tag{14}$$

We shall only consider next, the case where **S** is a tall matrix, meaning that there are more spectral points than sources (very common in practice). Given the spiky nature of Raman spectra, **S** is full column rank with high probability, implying $k_{\mathbf{S}}=N$. Kruskal's condition can thus be re-written as:

$$k_{\mathbf{B}} + k_{\mathbf{P}} \geq N+2. \tag{15}$$

Given the size of matrices **B** and **P**, and knowing that the Kruskal-rank of a matrix is upper bounded by its classical rank, the only possible solution to inequality (Eq. (15)) is $k_{\mathbf{P}}=2$ and $k_{\mathbf{B}}=N$. This means that, in order to have an unique factorization, every two sources must have different polarization behaviors and **B** (with $L \geq N$) has to be full column rank. Thus, in practice, the CP model (Eq. (13)) is identifiable in most cases, provided that more acquisition points than sources are used.

4.3. Fitting the spatial diversity data

Most methods for fitting the three-way CP model are derived from the Alternating Least Squares (ALS) regression which consists in estimating iteratively one matrix by fixing the two others [13,24]. As shown in the previous subsection, this factorization is unique provided that some mild conditions are satisfied. However, the direct use of ALS can be impractical and problematic, since it usually suffers from linear convergence, and is occasionally sensitive to local minima. To avoid these problems, several algorithms have been proposed lately. In Ref. [25] an enhanced line search (ELS) is proposed to accelerate the convergence of ALS. The COMFAC algorithm introduced in Ref. [26] uses more sophisticated initializations to achieve fast, accurate convergence for factorization of trilinear arrays. Given the nature of the data, it is also natural to impose non-negativity constraints on the matrices to estimate and thereby facilitate the interpretation of the results. This can be done similarly to the bilinear case (see Algorithm 1). An optimized nonnegative algorithm for three-way factorization, used in this paper to illustrate the proposed approach, can be found in the Matlab *N-way toolbox* developed by Bro and Anderson and freely available at: http://www.mathworks.com/matlabcentral/fileexchange/1088-the-n-way-toolbox.

In order to estimate the matrices of this trilinear model one could also use one of the algorithms for nonnegative bilinear factorization mentioned in Subsection 3.3 and apply it on an unfolded version of the data. This implies that, to ensure unicity on the decomposition, additional constraints on the sources and/or mixing coefficients must be made, not always physically justified. In this context, the main

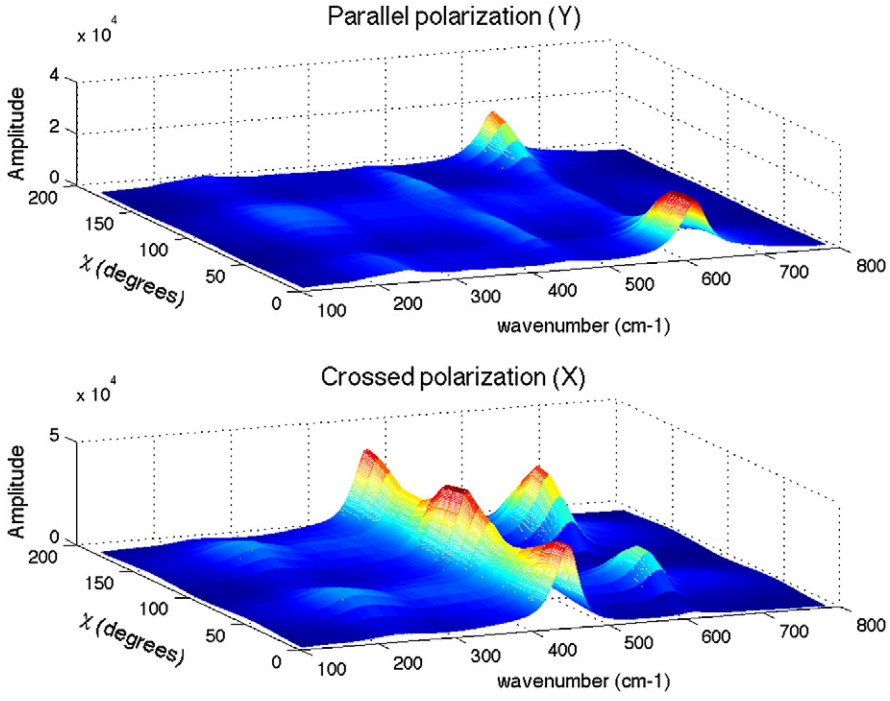

Fig. 6. Polarized Raman data versus rotational angle χ for rutile TiO_2 *(110)* single crystal.

advantage of the trilinear algorithms over the bilinear ones is the conservation of the intrinsic structure of the data as generated by the underlying phenomena.

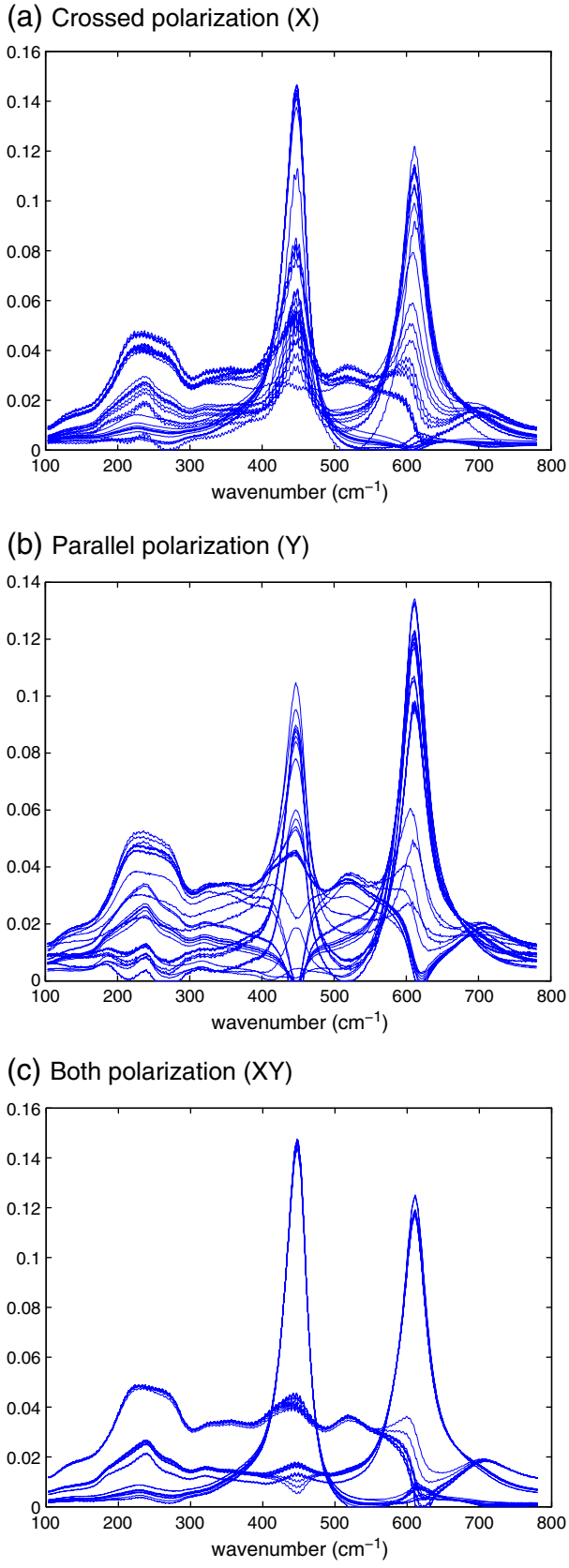

Fig. 7. Source spectra estimation by NMF (15 runs).

5. Results

In this section we illustrate the proposed approaches on polarized Raman spectra. The rotational diversity was explored using TiO_2 rutile single crystal and the spatial diversity Raman spectra were collected using a mixture of $CaCO_3$ powders with two polymorphs, aragonite and calcite.

5.1. Results for rotational diversity data

The approach presented in Section 3 was applied to a rutile TiO_2 crystal, as shown in Fig. 1. The crystallographic face (110) (Hermann–Mauguin international crystallographic symbols) is analyzed. The sample is rotated with respect to Z-axis only, meaning $\boldsymbol{\theta} = (0, 0, \chi)$. Fig. 6 presents the acquired polarized data for the parallel and crossed polarizations (matrices $\mathbf{D}_Y$ and $\mathbf{D}_X$ in Eq. (4)). The data was acquired in a spectral range of $100\,\mathrm{cm}^{-1} - 800\,\mathrm{cm}^{-1}$ with an angular rotation step of 10° between 0° and 190°.

In the case of TiO_2, four Raman active modes denoted as A_{1g}, E_g, B_{1g} and B_{2g} (Mulliken symbols for symmetry groups [1]) are expected from theory. However, the B_{2g} mode at $826\,\mathrm{cm}^{-1}$ is out of the spectral window used in the present work (and anyway the B_{2g} has a very low Raman crossed section and is often not detected). The B_{1g} mode with the (110) oriented crystal plane is silent either in parallel or crossed

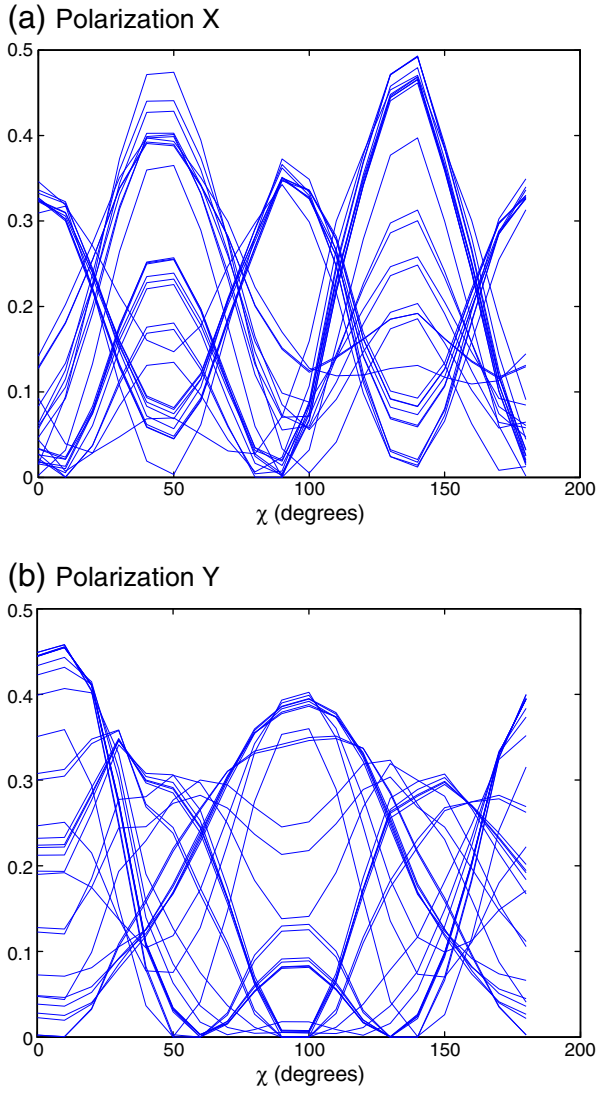

Fig. 8. Estimated coefficients by NMF for each polarization data set separately.

polarizations (the same calculation exposed for A_{1g} and E_g modes in Appendix A would show that B_{1g} mode is silent in our working conditions). Consequently, one can expect two Raman active modes, *i.e.* two sources, in the data collected here. Nevertheless, three sources are necessary to properly describe the data, as indicated by the magnitude analysis of the singular values of data matrices $\mathbf{D}_X$, $\mathbf{D}_Y$ and $\mathbf{D}$. A theoretical explanation for the presence of this third source is provided latter in this section.

First we illustrate the effect of the joint use of the crossed and parallel polarization data sets on the size reduction of the NMF admissible solutions set, as emphasized in Subsection 3.2. For the same data described earlier, the NMF algorithm [8] was used to estimate the three source vectors and the corresponding mixing coefficients. The two data sets were processed separately and jointly and the results are presented on Fig. 7 for the source spectra and on Figs. 8 and 9 for the mixing coefficients. To evaluate the size of the admissible solutions set we used 15 independent runs for each plot, with different random initial values for the matrices **A** and **S**. As one can see, by processing both polarization data sets jointly (Figs. 7(c) and 9) the admissible solution domain is largely reduced as compared to the case when only one polarization is used (Figs. 7(a),(b) and 8). These results validate the theoretical considerations presented in Subsection 3.2 and emphasize the utility of using both polarizations in Raman acquisitions.

Next, to illustrate the effect of the joint data processing on the estimation accuracy, the BPSS algorithm [11] is used, for the reasons presented in Subsection 3.3.

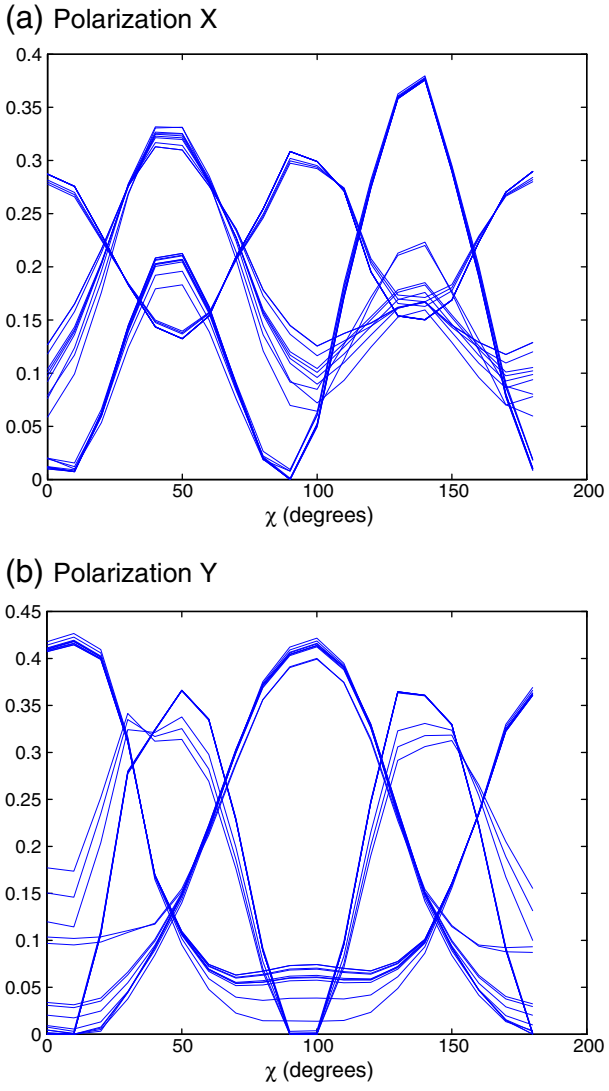

Fig. 9. Estimated coefficients by NMF for both polarization data sets jointly (15 runs).

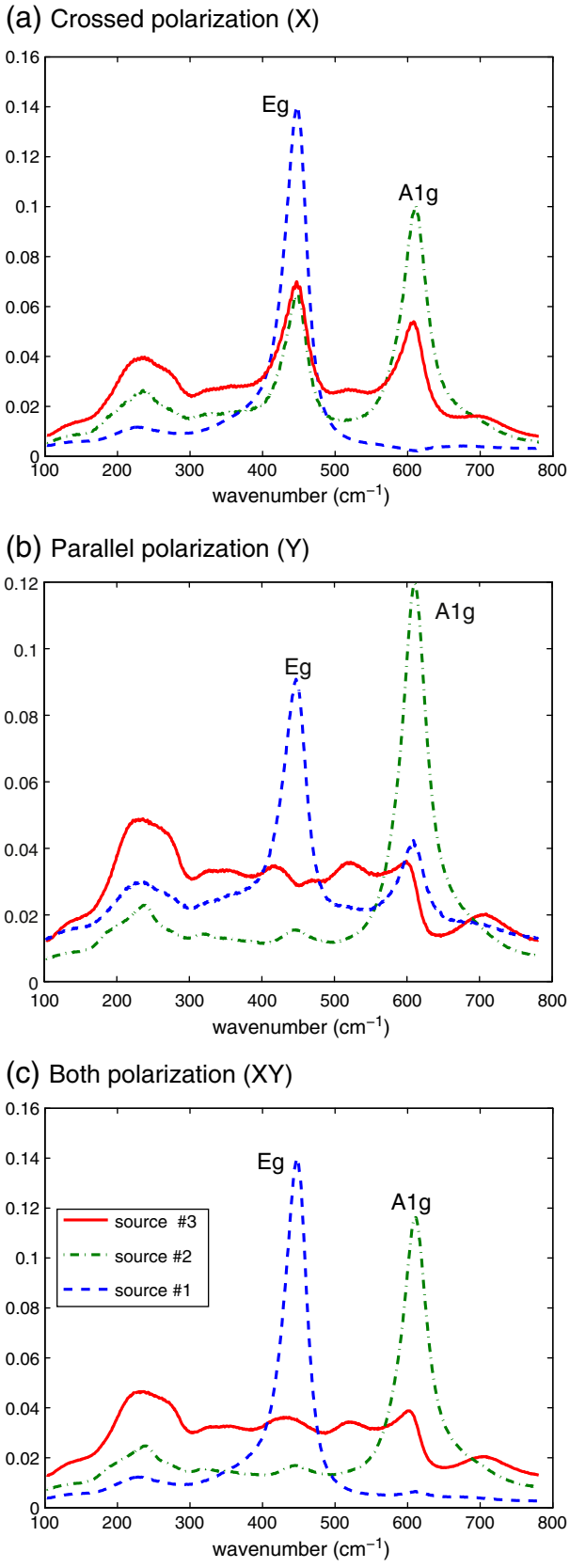

Fig. 10. Source spectra estimation by BPSS.

First, BPSS was applied on the concatenated data as in Eq. (7) and then on each of the polarized data sets independently, (according to Eq. (4)). The results for the joint processing of the polarizations are given on Fig. 10 (c) for the source spectra and on Fig. 12 for the mixing coefficients. Figs. 10(a) and (b) and 11 plots the estimated spectra and mixing coefficients, respectively using only the parallel or the crossed polarization data. Three sources are identified: one (#1) with the main peak at 440 cm^{-1} corresponding physically to the vibrational mode E_g, another (#2) at 610 cm^{-1} corresponding to the mode A_{1g} and a third one (#3) that is rather unexpected from the theoretical considerations exposed above. Indeed, one expect to find only two sources corresponding to the two Raman active modes A_{1g} and E_g. In fact, the spectral shape of source #3 corresponds to second-order Raman active mode and not to fundamental vibrational modes. This second-order mode has a structured shape (coming from the density of phonon states in rutile material) already observed and a complex behavior towards rotational diversity [27]. It is thought to be a harmonic or combination band of lower frequency fundamental acoustic modes that are silent in Raman spectroscopy (but their combination becomes Raman active due to symmetry consideration and spectroscopic rules). This is therefore a nice success of our approach to have revealed the existence of this second-order mode as a third source and to have retrieved its complex structure experimentally evidenced by Porto et al. [27].

One can see that the use of the two polarizations jointly improves the results of the bilinear factorization. This is especially visible on the source spectra, where the polarization information allows a more accurate separation of source contributions. For example, on Fig. 10 (c), source #1 is clearly concentrated at a single wavenumber (440 cm^{-1}), while on Fig. 10 (b) it presents an additional peak at the wavenumber corresponding to source #2. Similar remarks can be made for the two other sources in Fig. 10 (a).

The advantage of using the polarized data jointly is also visible on the mixing coefficients. For example, if we look at the crossed polarization data in Fig. 6 (bottom plot, near 440 cm^{-1}), one can see that the E_g mode, *i.e.* source #1, presents an offset for reasons that will be explained latter. If both datasets are used, the aforementioned characteristic is successfully recovered (Fig. 12 (a)) while this is not the case if the crossed polarization data is processed independently (Fig. 11 (a)). Similar remarks can be made for the other mixing coefficients and polarization dataset. In theory, the mixing coefficients of the two data sets (Fig. 12) are theoretically proportional to $\cos^2(2\chi)$ and $\sin^2(2\chi)$, respectively as shown in Appendix A. Therefore, they should pass by zero periodically. This is not the case for our data and a possible explanation to this fact is the electronic resonance phenomena which adds a baseline to the observed sources. Another possible explanation comes from the fact that we used a $\times 50$ optical

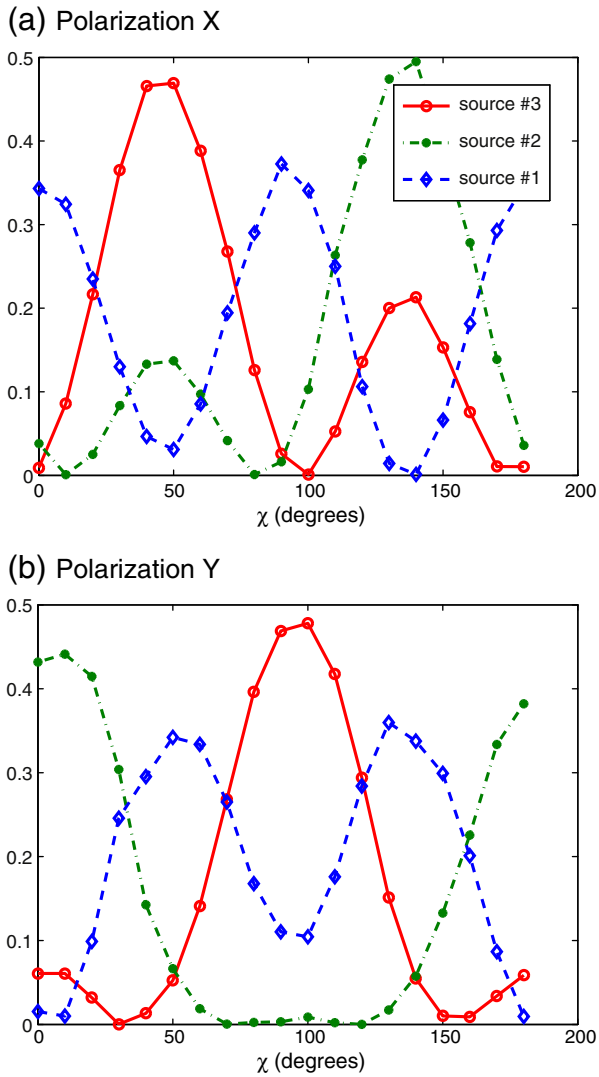

Fig. 11. Estimated coefficients by BPSS for each polarization data set separately.

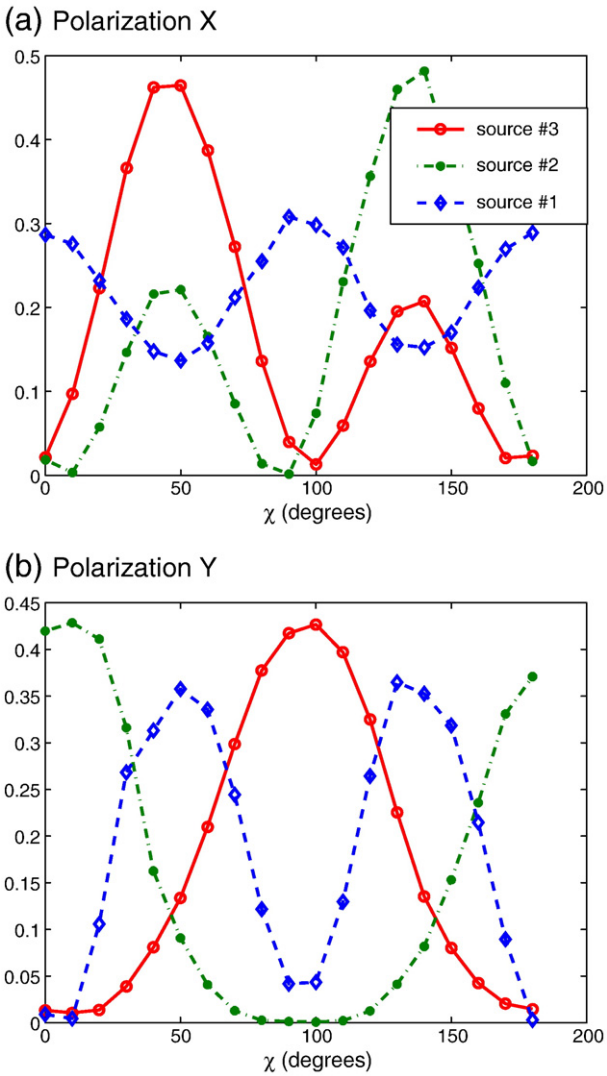

Fig. 12. Estimated coefficients by BPSS for both polarization data sets jointly.

objective with a numerical aperture of 0.55. The numerical aperture of this objective (0.55) was high enough to possibly induce a small contribution of Raman scattered light on the z-axis, responsible for such an offset.

5.2. Results for spatial diversity data

In this section, we analyze a mixture of two polymorphs of $CaCO_3$ having a distinct crystallographic structure. Though the Raman active modes involve similar atomic displacements, the change of the crystal symmetry produces significant separation of the Raman peaks for these two polymorphs. Some peaks are overlapped (for instance, around 700 cm^{-1}) but others are clearly well separated. Therefore, one source is classically viewed as the entire Raman spectrum of one polymorph in this section. This is different from the definition of sources adopted for the rotational diversity data model and leads to the trilinear mixture model.

For the illustration of the trilinear data model, we used a calcite crystal of several micrometers in diameter grown on an aragonite substrate. The polycrystalline sample of aragonite was made according to the process described in Ref. [28]. During the crystallization, calcite crystals (with an average size of several micrometers) were also grown as impurities. After filtration, we obtained some calcite crystals deposited randomly at the surface of the compacted aragonite powder. Such a place was chosen for testing our signal processing approach of polarized Raman mapping. The Raman spectra of pure aragonite and calcite samples are well known and have been presented previously in Ref. [28]. A spatial grid of 8×9 with a spatial step of 1 μm was read on crossed and parallel polarizations. The 2×72 resulting spectra are presented in Fig. 13 (a) and (b). The spectral range was $100-900$ cm^{-1}. In this case a source is no longer assimilated with one vibrational mode but rather with the totality of spectral peaks characterizing calcite or aragonite.

The data was processed using the PARAFAC decomposition algorithm with non-negativity constraints described in subsection 4.3. The estimated spectral signatures and mixing coefficients for the two crystalline varieties of $CaCO_3$ are presented on Figs. 14 and 15, respectively. As one can see in Fig. 14 the spectral signatures of the two sources are well recovered, in perfect agreement with the literature [28]. The fact that there are a lot of zero-values in the estimated spectra is due to negative values present in the analyzed data (see Fig. 13) as a side effect of the baseline removal in the preprocessing steps. The estimation of the mixing coefficients is also accurate, allowing to plot low resolution maps of the aragonite and calcite concentrations (Fig. 15 (a) and (b)), matching the visual image obtained in the microscope oculars. The concentration maps reported in Fig. 15 are also coherent with the fact that the diameter of the laser spot was around 2 micrometers and the size of the calcite crystal was a few micrometers. The size of the calcite single crystal is bigger than the laser spot and the crystal orientation is fixed. Therefore, this source obeys the model hypothesis stated in Section 4. The second source corresponds to aggregates of nano-crystals of aragonite polymorph, which are randomly oriented, and of size quite inferior to the laser spot. Thus, this second source also satisfies the model hypothesis.

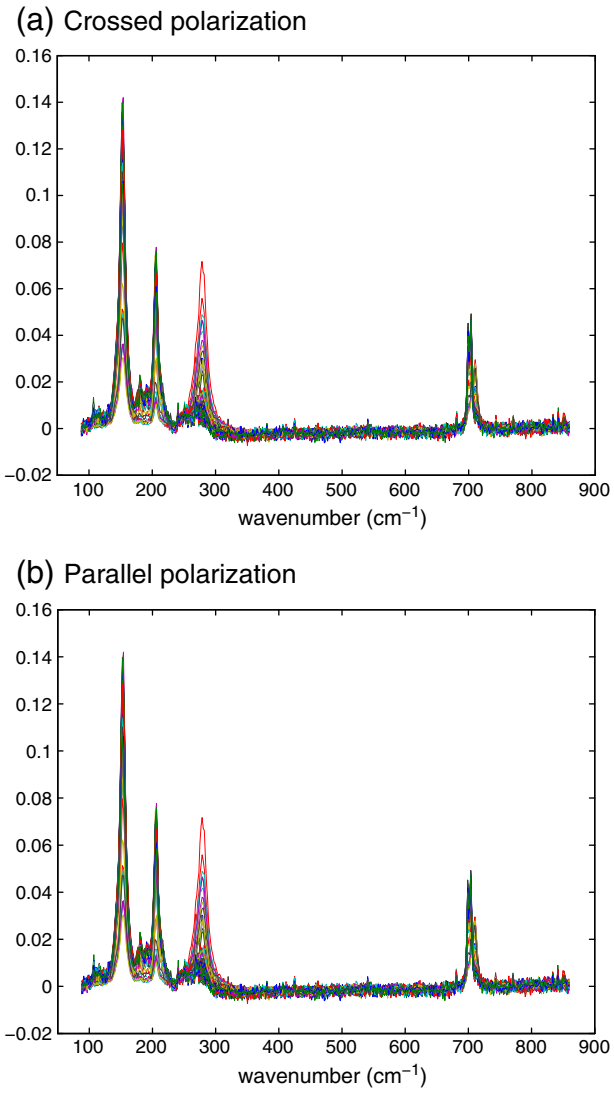

Fig. 13. Polarized data for $CaCO_3$.

6. Conclusions

We proposed in this paper two approaches for dealing jointly with the crossed and parallel polarization data in Raman spectroscopy. A bilinear and a trilinear model were introduced for polarized Raman spectroscopy data with rotational and spatial diversity, respectively. We showed that, besides improving source estimation accuracy, the joint use of polarization information reduces the size of the admissible solutions set for rotational diversity data and ensures mixture identifiability in Raman imaging. The proposed approaches were validated on real TiO_2 and $CaCO_3$ spectra. These first results highlight the importance of using both crossed and parallel polarizations in Raman acquisitions and should serve as basis for future experimental protocols allowing further developments in Raman imaging and the estimation of the polarizability tensor components.

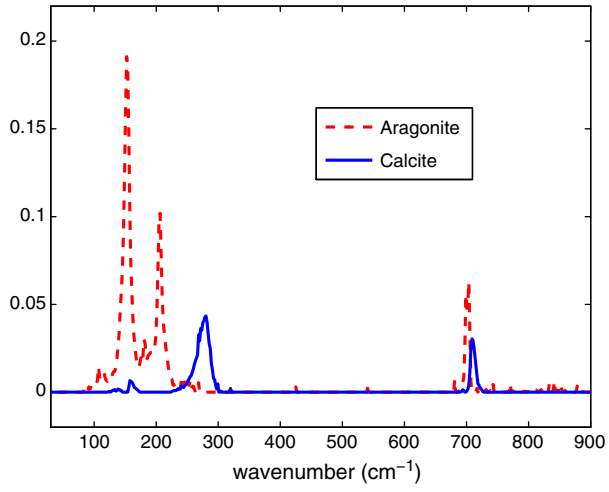

Fig. 14. Spectra separation result $CaCO_3$.

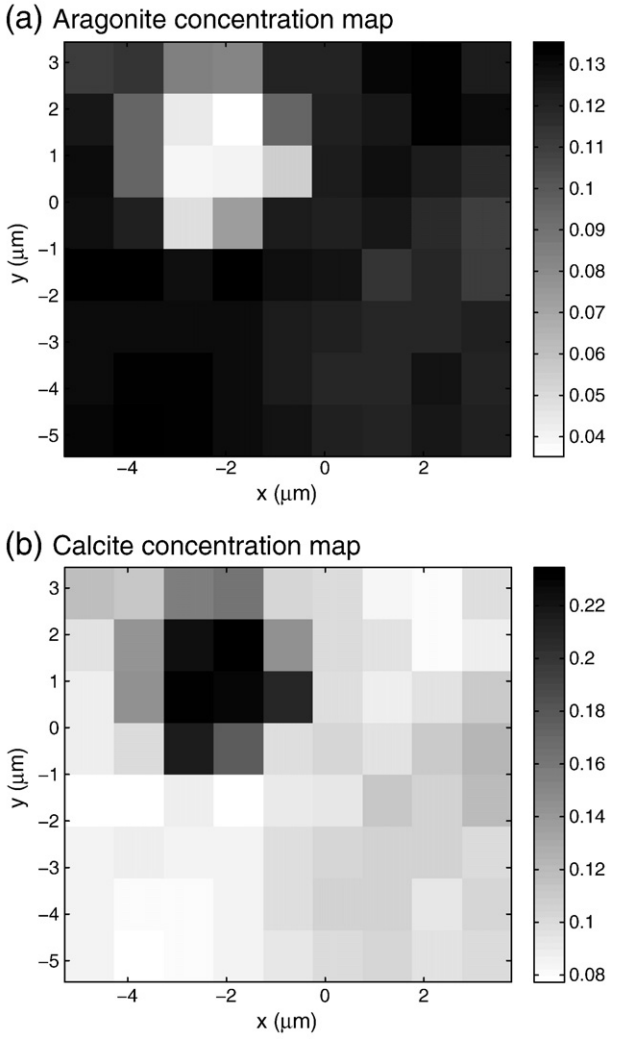

Fig. 15. Concentration maps for the $CaCO_3$ sample.

Funding source

This work was supported through a financial grant delivered by the CCOS Lorrain and Region Lorraine.

Appendix A. Theoretical calculation of the intensity of the Raman active vibrations of TiO_2 rutile for the (110) crystal plane versus the rotational angle

The rutile structure of TiO_2 has four Raman active vibrational modes noted A_{1g},E_g,B_{1g} and B_{2g} [27]. The tensor components for each mode are:

$$\boldsymbol{\alpha}_{A_{1g}} = \begin{pmatrix} \alpha_1 & 0 & 0 \\ 0 & \alpha_1 & 0 \\ 0 & 0 & \alpha_2 \end{pmatrix},$$

$$\boldsymbol{\alpha}_{E_g} = \begin{pmatrix} 0 & 0 & 0 \\ 0 & 0 & \alpha_3 \\ 0 & \alpha_3 & 0 \end{pmatrix}, \quad \begin{pmatrix} 0 & 0 & \alpha_3 \\ 0 & 0 & 0 \\ \alpha_3 & 0 & 0 \end{pmatrix},$$

(This mode is doubly degenerated.)

$$\boldsymbol{\alpha}_{B_{1g}} = \begin{pmatrix} \alpha_4 & 0 & 0 \\ 0 & -\alpha_4 & 0 \\ 0 & 0 & 0 \end{pmatrix},$$

$$\boldsymbol{\alpha}_{B_{2g}} = \begin{pmatrix} 0 & \alpha_5 & 0 \\ \alpha_5 & 0 & 0 \\ 0 & 0 & 0 \end{pmatrix}.$$

The laser polarization was fixed along the *Y*-axis of the laboratory frame plotted in Fig. 1. The analyzer was then either along the *Y*-axis (parallel polarizations) or the *X*-axis (crossed polarizations). The wave vector of the laser radiation was along *Z*.

The expressions for the polarizability tensors are given in the coordinate system (O,x,y,z) attached to the analyzed sample. For the (110) crystal plane, the use of a rotation matrix $\mathbf{R}'$ is needed in order to align the crystal plane (110) parallel to the *(OXY)* laboratory plane. This way, an intermediate frame (O,x',y',z') is defined and the tensor components in this frame are given by:

$$\boldsymbol{\alpha}_{(O,x',y',z')} = \mathbf{R}'^{-1}\boldsymbol{\alpha}\mathbf{R} \tag{A.1}$$

with

$$\mathbf{R}' = \begin{pmatrix} 0 & -\frac{\sqrt{2}}{2} & \frac{\sqrt{2}}{2} \\ 0 & \frac{\sqrt{2}}{2} & \frac{\sqrt{2}}{2} \\ -1 & 0 & 0 \end{pmatrix}. \tag{A.2}$$

Another rotation matrix $\mathbf{R}$, corresponding to rotational angle variation χ around the *Z*-axis, allows to express the measurements in the laboratory (O,X,Y,Z) coordinate system:

$$\mathbf{R} = \begin{pmatrix} cos\chi & sin\chi & 0 \\ -sin\chi & cos\chi & 0 \\ 0 & 0 & 1 \end{pmatrix}. \tag{A.3}$$

Thus, the new tensor components in the (O,X,Y,Z) frame are given by:

$$\boldsymbol{\alpha}_{(O,X,Y,Z)} = \mathbf{R}^{-1}\alpha_{(O,x',y',z')}\mathbf{R}. \tag{A.4}$$

We applied these equations to the A_{1g} and E_g modes that are found within the spectral window explored in this article.

A.1. E_g mode ($450\ cm^{-1}$)

For this doubly degenerated mode the following two results were obtained:

$$\boldsymbol{\alpha}_{(O,X,Y,Z)} = \begin{pmatrix} \sqrt{2}\,cos(\chi)\,sin(\chi)\alpha_3 & \frac{\sqrt{2}}{2}\left(sin^2(\chi) - cos^2(\chi)\right)\alpha_3 & -\frac{\sqrt{2}}{2}cos(\chi)\alpha_3 \\ \frac{\sqrt{2}}{2}\left(sin^2(\chi) - cos^2(\chi)\right)\alpha_3 & -\sqrt{2}\,cos(\chi)\,sin(\chi)\alpha_3 & -\frac{\sqrt{2}}{2}sin(\chi)\alpha_3 \\ -\frac{\sqrt{2}}{2}cos(\chi)\alpha_3 & -\frac{\sqrt{2}}{2}sin(\chi)\alpha_3 & 0 \end{pmatrix} \tag{A.5}$$

and

$$\boldsymbol{\alpha}_{(O,X,Y,Z)} = \begin{pmatrix} -\sqrt{2}\,cos(\chi)\,sin(\chi)\alpha_3 & \frac{\sqrt{2}}{2}\left(cos^2(\chi) - sin^2(\chi)\right)\alpha_3 & -\frac{\sqrt{2}}{2}cos(\chi)\alpha_3 \\ \frac{\sqrt{2}}{2}\left(cos^2(\chi) - sin^2(\chi)\right)\alpha_3 & \sqrt{2}\,cos(\chi)\,sin(\chi)\alpha_3 & -\frac{\sqrt{2}}{2}sin(\chi)\alpha_3 \\ -\frac{\sqrt{2}}{2}cos(\chi)\alpha_3 & -\frac{\sqrt{2}}{2}sin(\chi)\alpha_3 & 0 \end{pmatrix}. \tag{A.6}$$

The electric field of the incident laser is given by $\mathbf{e} = (0 \quad e_Y \quad 0)^T$ and the induced polarization is:

$$\mathbf{p} = \alpha_{(O,X,Y,Z)}\mathbf{e}. \tag{A.7}$$

The Raman intensity $\mathbf{i}$ is proportional to the square of the induced polarization. Thus we can predict for the doubly degenerated E_g mode:

- for parallel polarizations (YY): $i_Y \propto \sin^2(2\chi)\alpha_3 e_Y^2$
- for crossed polarizations (XY): $i_X \propto \cos^2(2\chi)\alpha_3 e_Y^2$.

Normally the E_g mode in parallel polarizations should be equal to zero for a rotational angle of 90°. Fig. 12(b) shows that there is a small residual component near this angle value, which is discussed in the

text. The variations for the crossed polarization are coherent with the theoretical predictions excepting for the general offset of the curve in Fig. 12(a) (source #1).

A.2. A_{1g} mode (612 cm^{-1})

For the A_{1g} mode, the calculations give the following results:

$$\boldsymbol{\alpha}_{(O,X,Y,Z)} = \begin{pmatrix} cos^2(\chi)\alpha_2 + sin^2(\chi)\alpha_1 & cos(\chi)\,sin(\chi)(\alpha_2-\alpha_1) & 0 \\ cos(\chi)\,sin(\chi)(\alpha_2-\alpha_1) & cos^2(\chi)\alpha_1 + sin^2(\chi)\alpha_2 & 0 \\ 0 & 0 & \alpha_1 \end{pmatrix} \quad (A.7)$$

- for parallel polarizations (YY): $i_Y \propto (\alpha_2 \sin^2\chi + \alpha_1 \cos^2\chi)e_Y^2$
- for crossed polarizations (XY): $i_X \propto \sin^2(2\chi)(\alpha_2-\alpha_1)^2 e_Y^2$.

The variations observed in Fig. 12 (a) and (b) for source #2 are in good agreement with these predictions. The fact that in parallel polarizations, source #2 is almost zero for a rotational angle of 90° indicates that the magnitude of α_2 is considerably smaller than the magnitude of α_1.

References

[1] D.A. Long, The Raman Effect: A Unified Treatment of the Theory of Raman Scattering by Molecules, John Wiley & Sons. Ltd, 2002.
[2] G. Turrell, Infrared and Raman Spectra of Crystals, Academic Press, 1972.
[3] S. Sobanska, G. Falgayrac, J. Laureyns, C. Brémard, Chemistry at level of individual aerosol particle using multivariate curve resolution of confocal Raman image, Spectrochimica Acta Part A 64 (2006) 1102–1109.
[4] C. Jimenez, T. Caroff, A. Bartasyte, S. Margueron, A. Abrutis, O. Chaix-Pluchery, F. Weiss, Raman study of the CeO_2 texture as buffer layer in the $CeO_2/La_2Zr_2O_7$/Ni architecture for coated conductors, Applied Spectroscopy 63 (2009) 401.
[5] Y. Batonneau, C. Brémard, J. Laureyns, J.-C. Merlin, W. Windig, Polarization effects of confocal Raman microspectrometry of crystal powders using interactive self-modeling analysis, The Journal of Physical Chemistry B 107 (2003) 1502–1513.
[6] R. Tauler, B. Kowalski, S. Fleming, Multivariate curve resolution applied to spectral data from multiple runs of an industrial process, Analytical Chemistry 65 (15) (1993) 2040–2047.
[7] P. Paatero, U. Tapper, Positive matrix factorization: a nonnegative factor model with optimal utilization of error estimates of data values, Environmetrics 5 (1994) 111–126.
[8] D.D. Lee, H.S. Seung, Learning the parts of objects by non-negative matrix factorization, Nature 401 (6755) (1999) 788–791.
[9] W. Windig, J. Guilment, Interactive self-modeling mixture analysis, Analytical Chemistry 63 (14) (1991) 1425–1432.
[10] S. Moussaoui, D. Brie, C. Carteret, A. Mohammad-Djafari, Bayesian analysis of spectral mixture data using Markov Chain Monte Carlo methods, Chemometrics and Intelligent Laboratory Systems (2006) 137–148.
[11] S. Moussaoui, D. Brie, A. Mohammad-Djafari, C. Carteret, Separation of non-negative mixture of non-negative sources using a Bayesian approach and MCMC sampling, IEEE Transactions on Signal Processing 54 (11) (2006) 4133–4145.
[12] J.D. Carroll, J.-J. Chang, Analysis of individual differences in multidimensional scaling via an N-way generalization of "Eckardt-Yong" decomposition, Psychometrika 35 (3) (1970) 283–319.
[13] R. Harshman, Foundations of the PARAFAC procedure: model and conditions for an 'explanatory' multi-mode factor analysis, UCLA Working Papers Phonetics 16 (1970) 1–84.
[14] J. Jaumot, J. Menezes, R. Tauler, Quality assessment of the results obtained by multivariate curve resolution analysis of multiple runs of gasoline blending processes, Journal of Chemometrics 20 (2006) 54–67.
[15] C. Ruckebusch, A. De Juan, L. Duponchel, J. Huvenne, Matrix augmentation for breaking rank-deficiency: a case study, Chemometrics and Intelligent Laboratory Systems 80 (2006) 209–214.
[16] J. Chen, The nonnegative rank factorizations of nonnegative matrices, Linear Algebra and its Applications 62 (1984) 207–217.
[17] D. Donoho, V. Stodden, When does non-negative matrix factorization give correct decomposition into parts? Advances in Neural Information Processing, Vol. 16, 2003.
[18] H. Laurberg, M.G. Christensen, M.D. Plumbley, K.L. Hansen, S.H. Jensen, Theorems on positive data: on the uniqueness of NMF, Computational Intelligence and Neuroscience (2008) 764206.
[19] S. Moussaoui, D. Brie, J. Idier, Non-negative source separation: range of admissible solutions and conditions for the uniqueness of the solution, Proc. IEEE International Conference on Acoustics, Speech and Signal Processing, Philadelphia, USA, 2005.
[20] M. Vosough, C. Mason, R. Tauler, M. Jalali-Heravi, M. Maeder, On rotational ambiguity in model-free analyses of multivariate data, Journal of Chemometrics 20 (2006) 302–310.
[21] P.O. Hoyer, Non-negative matrix factorization with sparsness constraints, Journal of Machine Learning Research 5 (2004) 1457–1469.
[22] A. Cichocki, R. Zdunek, S. Amari, Nonnegative matrix and tensor factorization, IEEE Signal Processing Magazine (2008) 142–145.
[23] J. Kruskal, Three-way arrays: rank and uniqueness of trilinear decompositions with application to arithmetic complexity and statistics, Linear Algebra and its Applications 18 (1977) 95–138.
[24] A. Smilde, R. Bro, P. Gheladi, Multi-Way Analysis. Applications in the Chemical Sciences, Wiley, Chichester, U.K, 2004.
[25] M. Rajih, P. Comon, Enhanced line search: a novel method to accelerate PARAFAC, SIAM Journal on Matrix Analysis and Applications 30 (3) (2008) 1128–1147.
[26] R. Bro, N. Sidiropoulos, G. Giannakis, A fast least squares algorithm for separating trilinear mixtures, Proc. Int. Workshop Independent Component Analysis and Blind Signal Separation (ICA), Aussois, France, 1999.
[27] S. Porto, P. Fleury, T. Damen, Raman spectra of TiO_2, MgF_2, ZnF_2, FeF_2 and MnF_2, Physical Review 154 (1967) 522–526.
[28] C. Carteret, A. Dandeu, S. Moussaoui, H. Muhr, B. Humbert, E. Plasari, Polymorphism studied by lattice phonon Raman spectroscopy and statistical mixture analysis method: application to calcium carbonate polymorphs during batch crystallization, Crystal Growth and Design 9 (2009) 807–812.